Complete characterization of the directly implementable quantum gates used in the IBM quantum processors

Abhishek Shukla [a,b], Mitali Sisodia [a], Anirban Pathak [a,*]

[a] *Jaypee Institute of Information Technology, A 10, Sector 62, Noida, UP 201307, India*
[b] *Department of Applied Physics, The Hebrew University of Jerusalem, Jerusalem 9190401, Israel*

ABSTRACT

Quantum process tomography (QPT) of each directly implementable quantum gate used in the IBM quantum processors is performed to compute gate error in order to check viability of complex quantum operations in the superconductivity-based quantum computers introduced by IBM. QPT of C-NOT gates is performed for three configurations available in IBM QX4. For the other allowed gates QPT have been performed for every allowed position (i.e., by placing the gates in different qubit lines) for IBM QX4 architecture, and thus, gate fidelities are obtained. Gate fidelities are observed to be lower than the corresponding values obtained in the other technologies, like NMR. Further, gate fidelities for all the single-qubit gates are obtained for IBM QX2 architecture by placing the gates in the third qubit line (q[2]). It's observed that the IBM QX4 architecture yields better gate fidelity compared to IBM QX2 in all cases except Y gate.

1. Introduction

Experimental implementation of any quantum information processing task is all about initializing the system qubits to an aptly chosen quantum state followed by manipulating the initial state through a set of unitary and/or non-unitary quantum operations to obtain the desired output state and ultimately measuring that to obtain the expectation value of the desired observable. Implementation of a multi-qubit unitary quantum operation of arbitrary dimension requires application of local and non-local operations (quantum gates). Local operations are usually realized by means of external control fields, whereas the non-local operations are implemented by exploiting two-body interaction. The perfect realization of these quantum operations are possible only in the ideal scenario. In practice, the accuracy with which a quantum operation can be realized is limited by imperfect designing and implementation errors, and environmental effects. To circumvent or to suppress these factors which reduces accuracy, we need to design robust control fields. In order to design control fields robust against environmental effects, design errors and implementation errors, it becomes imperative to characterize the control fields. The procedure of characterizing quantum operation and hence control fields is known as quantum process tomography (QPT) [1,2]. It (i.e.,

QPT) inherently involves QST [3]. This is so because a quantum operation (except the selective measurements) linearly maps input density matrix to output density matrix. The procedure of QPT involves initializing system-qubits in an aptly chosen density matrix basis, followed by application of a process on these basis states and ultimately characterizing output quantum states through QST.

The idea of QPT was introduced in 1997, but the first experimental demonstration of QPT was done in 2001 using a nuclear magnetic resonance-(NMR) based architecture [4,5]. Since then QPT has been performed using various quantum computing architectures, including architectures based on linear optics [6–9], ion traps [10,11], superconductivity [12–17], and nitrogen vacancy (NV) center [18,19]. Until now, a large number of modified and new methods for QPT have also been devised. Most common methods are like ancilla-assisted quantum process tomography (AAQPT) which reduces the number of experiments required to be done for the complete characterization of a quantum operation by exploiting ancillary qubits [7], single-scan quantum process tomography which allows characterization of a process in one scan and thus allows to tomograph dynamical process [20], adaptive process tomography which utilizes the advantages of the adaptive strategies applied to state reconstruction, and allows to tomograph a process with ultimate bound of precision for state tomography [21]. These schemes for QPT are demanding in the sense that either they require to perform a large number of experiments or they require a large amount of resources [1,7,20]. This is why a set

* Corresponding author.
E-mail address: anirbanpathak@yahoo.co.in (A. Pathak).

of simplified QPT schemes have been developed. Such a scheme exploits prior knowledge of type of interaction involved in generating the dynamics and hence remove scaling problem involved in a standard method for QPT [22,23] and that in the recently devised bootstrap tomography [24,25]. Another method which is based on error detection and does not involve QST is direct characterization of quantum dynamics [26].

In the last few years, QPT has played an extremely important role in the experimental quantum computing and communication, as it has led to the procedures for designing more precise and robust control fields. This is what motivated us to perform QPT for the quantum operations that are implemented in the different architectures of 5 qubit IBM quantum computers (i.e., in IBM QX2 and IBM QX4). Here, it may be apt to note that the IBM Corporation has recently introduced a quantum computing platform [27] with two five-qubit quantum processors [28] accessible through the cloud to the registered users. Quantum information processing (QIP) on these processors involves initialization, manipulation, and measurement of Transmon qubits by utilizing superconductivity-based QIP architecture. A QIP task in an IBM quantum processor may involve a set of unitary and non-unitary operations (measurements). Unitary operations in the IBM quantum computers is governed by a quantum circuit comprised of single-qubit and multi-qubit gates selected from the Clifford+T gate library. In order to examine the goodness of these gates, in what follows, we have completely characterized the quantum gates using standard method of QPT. This investigation is further motivated by the fact that the IBM quantum computers have already been utilized to implement various quantum computing (e.g., [29–31]) and communication [32,33] tasks and in many of these works quantum state tomography (QST) has been performed and quantum state fidelity has been reported to be low or moderate [34,35]. This is in sharp contrast to the fact that the fidelities of the gates given in the IBM quantum processors' backend information [36] are very high. Interestingly, no serious effort has yet been made to perform QPT of these gates and to investigate the origin of low or moderate quantum state fidelity as a consequence of the imperfection of the implemented gates (i.e., low gate fidelity). Present work aims to look into this particular perspective, and thus to establish that the present technology would require considerable improvement in gate fidelity to achieve the desired scalability.

The rest of the paper is organized in the following way. In Sec. 2, we briefly describe the theory of QPT. In Sec. 3, we present a scheme for performing QPT on IBM QX4 and IBM QX2 quantum processors. Our results of QPT performed on IBM quantum processors are presented and analyzed in Sec. 4. The paper is finally concluded in Sec. 5.

2. Theory of QPT

A general quantum operation $\epsilon(\rho)$, linearly maps a density matrix ρ into another density matrix $\rho\prime$ such that $\rho\prime = \epsilon(\rho)$. Here, ρ is the input density matrix and $\rho\prime$ is the output density matrix. In the following, for the sake of completeness, we briefly describe the theoretical framework of QPT [1,2,37]. In operator sum representation, output density matrix $\rho\prime$ can be written as

$$\epsilon(\rho) = \sum_k E_k \rho E_k^\dagger, \tag{1}$$

where, $\{E_k\}$ are Kraus operators such that $\sum_k E_k^\dagger E_k = \mathbb{I}$ [37]. Determining quantum operation ϵ is equivalent to determining a set of operational elements $\{E_k\}$. In practice, determining these operators correspond to determining a set of complex numbers for each operational element E_k. Thus, expanding E_k in terms of fixed set

of operators $\{\tilde{E}_m\}$ such as $E_k = \sum_m e_{km}\tilde{E}_m$, where $\tilde{E}_m$ forms an operator basis.

$$\epsilon(\rho) = \sum_{(m,n)} \chi_{mn} \tilde{E}_m \rho \tilde{E}_n^\dagger. \tag{2}$$

Here, $\chi_{mn} = e_{km}e_{km}{}^*$ are elements of a positive Hermitian matrix known as χ matrix. Matrix χ completely characterizes the corresponding quantum process expanded in operator basis $\{\tilde{E}_m\}$. This is why χ matrix is also known as process matrix. Let's choose $\{\rho_j\}$ as the basis in which a density matrix of arbitrary dimension $d = 2^n$ can be expanded, where $1 \leq j \leq d^2$. Then,

$$\epsilon(\rho) = \sum_{(m,n)} \sum_j \chi_{mn} \tilde{E}_m \rho_j \tilde{E}_n^\dagger, \tag{3}$$

and $\epsilon(\rho_j)$ can be written as

$$\epsilon(\rho_j) = \sum_k \lambda_{jk} \rho_k. \tag{4}$$

Here, $\epsilon(\rho_j)$ is the experimental outcome obtained from the state tomography performed for the input state ρ_j and allows us to compute λ_{jk}, also comparison of Eq. (3) and Eq. (4) leads to the relation

$$\lambda_{jk} = \sum_{mn} \chi_{mn} \beta_{mn}^{jk}. \tag{5}$$

For given input density matrix ρ_j, output density matrix ρ_k, and basis operator $\tilde{E}_m$ β_{mn}^{jk} can be calculated using

$$\sum_k \beta_{mn}^{jk} \rho_k = \tilde{E}_m \rho_j \tilde{E}_n^\dagger. \tag{6}$$

While, λ_{jk} can be obtained from tomography results using Eq. (4). As inversion of β_{mn}^{jk} is guaranteed (see Ref. [37]), one can rewrite Eq. (5) as follows.

$$\chi = \beta^{-1}\lambda. \tag{7}$$

Here, χ and λ are column vectors of dimension $d^4 \times 1$ containing elements χ_{mn} and λ_{jk} respectively, while β^{-1} is a matrix of dimension $d^4 \times d^4$. Matrix β is then constructed by arranging elements β_{mn}^{jk} for jk row-wise and mn column-wise. Keeping this theoretical framework in mind, in the following section, we will describe an explicit protocol for performing experimental QPT on the IBM quantum processors.

3. Experimental scheme for performing QPT on the IBM quantum processors

IBM quantum processors are based on superconducting Transmon qubits. Our experiments have been executed on IBM QX2 and IBM QX4 processors. Topology of superconducting qubits and allowed C-NOT operations in each of these architectures are given in [28]. Description of the architectures topology, type of qubits, means to manipulate them (control fields, transmission lines, and gate library), and measurement schemes have been provided in [36,38]. A useful summary of the architecture description is also available in [34,33]. Here we restrict ourselves from restating those information. However, for the sake of completeness, we provide important experimental parameters including Hamiltonian parameters and decoherence times for IBM QX2 and IBM QX4 processors in Table 1 and in Table 2, respectively. This is in accordance with the information provided by IBM in [36,38].

As explained in Sec. 1, method for QPT inherently involves QST. Procedure for performing QST on IBM's quantum processors is extensively described in an earlier work of ours [34]. In the following, we revisit the essential elements of QST.

Table 1

Details of the experimental parameters used in IBM quantum processor IBM QX2 as available on the website [36]. The first row is qubit index q[i] in IBM quantum computer. The second row shows resonance frequencies ω^R of corresponding read-out resonators. The qubit frequencies ω are given in the third column. Anharmonicity δ as provided in the fourth row, is a measure of information leakage out of the computational space. We can compute δ by taking the difference between two subsequent transition frequencies. The fifth and the sixth rows are qubit-cavity coupling strengths χ and coupling of the cavity to the environment κ for corresponding qubit. Longitudinal relaxation time (T_1) and Transverse relaxation time (T_2) are given in the seventh and the last rows, respectively.

Qubit number q[i]	q[0]	q[1]	q[2]	q[3]	q[4]
$\omega^R/2\pi$ (GHz)	6.530350	6.481848	6.436229	6.579431	6.530225
$\omega/2\pi$ (GHz)	5.2723	5.2145	5.0289	5.2971	5.0561
$\delta/2\pi$ (MHz)	−330.3	−331.9	−331.2	−329.4	−335.5
$\chi/2\pi$ (kHz)	476	395	428	412	339
$\kappa/2\pi$ (kHz)	523	489	415	515	480
$T_1(\mu s)$	53.04	63.94	52.08	51.78	55.80
$T_2(\mu s)$	48.50	35.07	89.73	60.93	84.18

Table 2

Details of the experimental parameters used in IBM quantum processor IBM QX4 as available as backend information in [38]. The first row is qubit index q[i] in IBM quantum computer. The second row shows resonance frequencies ω^R of corresponding read-out resonators. The qubit frequencies ω are given in the third column. Anharmonicity δ as provided in the fourth row, is a measure of information leakage out of the computational space. As before, δ can be calculated by taking the difference between two subsequent transition frequencies. The fifth and the sixth rows are qubit-cavity coupling strengths χ and coupling of the cavity to the environment κ for corresponding qubit. Longitudinal relaxation time (T_1) and Transverse relaxation time (T_2) are given in the seventh and the last rows respectively.

Qubit number q[i]	q[0]	q[1]	q[2]	q[3]	q[4]
$\omega^R/2\pi$ (GHz)	6.52396	6.48078	6.43875	6.58036	6.52698
$\omega/2\pi$ (GHz)	5.2461	5.3025	5.3562	5.4317	5.1824
$\delta/2\pi$ (MHz)	−330.1	−329.7	−323.0	−327.9	−332.5
$\chi/2\pi$ (kHz)	410	512	408	434	458
$T_1(\mu s)$	48.70	39.70	49.70	35.80	56.60
$T_2(\mu s)$	14.00	34.80	55.00	18.10	31.5

1. Prepare the density matrix which is to be tomographed.
2. Measure direct observables i.e., perform measurement in computational basis.
3. Transform unobservable elements to the directly observable elements by means of a unitary transformation followed by measurement in computational basis.
4. Apply Hadamard gate to transfer information encoded in $\{+, -\}$ basis to computational basis $\{0, 1\}$. Subsequently, perform measurement in Z (computational) basis for each qubit.
5. Apply $S^\dagger$ followed by Hadamard H to transfer information encoded in $\{|r^+\rangle = \frac{|0\rangle + i|1\rangle}{\sqrt{2}}, |r^-\rangle = \frac{|0\rangle - i|1\rangle}{\sqrt{2}}\}$ basis to computational basis $\{0, 1\}$. Subsequently, measure in Z basis for each qubit.
6. Collect probabilities from experimental outcomes and calculate expectation values of all observables constituting density matrix in Pauli basis.
7. Calculate $\langle A \rangle = \sum_i p_i e_i$, where p_i is the ith outcome of measurement and e_i is the ith eigen value of operator A.

Of course QST requires multiple experiments and the number of experiments to be performed increases with the dimension of the density matrix to be tomographed. Still it's a less complex task in comparison to QPT. This is one of the reasons that QST is reported in a handful of papers on IBM quantum computers [39,40,34] but QPT procedure has not yet been reported in any work. In IBM's quantum processor number of experiments required for QST using standard method scales as 3^n with number of qubits while total number of experiments required in QPT scales as $4^n 3^n$. This point

will be further clarified below as we would explain the procedure adopted here for performing the experiments required for QPT.

3.1. Single-qubit QPT

Following the procedure explained in Sec. 2, in what follows, we explain the procedure for QPT adopted here to perform complete characterization of single-qubit gates used in IBM QX2 and IBM QX4 quantum processors. A schematic diagram illustrating the procedure devised for the single-qubit process tomography for our choice of basis $\rho_i : \rho_1 = |0\rangle\langle 0|, \rho_2 = |0\rangle\langle 1|, \rho_3 = |1\rangle\langle 0|, \rho_4 = |1\rangle\langle 1|$ and fixed set of operators $\tilde{E}_m = \{\mathbb{I}, X, -iY, Z\}$ is shown in Fig. 1. Execution of single-qubit process tomography on IBM's quantum processors require following steps.

1. Initialize density matrix to the basis element ρ_1 by preparing qubit of interest q[i] to state $|0\rangle$.
2. Apply quantum process $\epsilon(\rho)$ on initial state $|0\rangle$.
3. Perform measurement in Z basis (direct observable) which reveals λ_{11} and λ_{14}.
4. Apply Hadamard gate to transfer information encoded in $\{+, -\}$ basis to computational basis $\{0, 1\}$. Subsequently, measure in Z basis.
5. Apply $S^\dagger$ followed by Hadamard H to transfer information encoded in $\{r^+, r^-\}$ basis to computational basis $\{0, 1\}$. Subsequently, measure in Z basis.
6. Use above two steps together to obtain λ_{12} and λ_{13}.
7. Repeat steps 1-5 for all ρ_i in order to get all λ_{ij}.
8. Compute β^{-1} using Eq. (6) for $\tilde{E}_m = \{\mathbb{I}, X, -iY, Z\}$.
9. Finally, calculate vector χ using Eq. (5) and thus reconstruct the process matrix χ.

In the above, points (3-5) describe method for QST, the three expriments, give the probabilities of the measurement outcomes in the X, Y, and Z-basis. Thus, three experiments are required for single-qubit QST. The matrix (β^{-1}) which maps QST outcomes λ_{jk} into χ matrix. The set of equations used to construct matrix β are linearly independent (with full rank) and well conditioned (condition number 1). During implementation of the above procedure for the experimental realization of QPT using IBM quantum processors one should be careful about a caveat, i.e., ρ_2 and ρ_3 are non-Hermitian so it is not possible to prepare them experimentally. In order to overcome this limitation, we have used a concept proposed in [37]. Specifically, we have performed two experiments as follows: (i) Prepare an initial state $|p\rangle\langle p| = (\frac{|0\rangle + |1\rangle}{\sqrt{2}})(\frac{\langle 0| + \langle 1|}{\sqrt{2}})$, apply operation ϵ, and tomograph the output state $\epsilon(|p\rangle\langle p|)$. (ii) Do the same experiment with the initial state $|m\rangle\langle m|$ and tomograph the output state $\epsilon(|m\rangle\langle m|)$. Here, state $|m\rangle = \frac{|0\rangle + i|1\rangle}{\sqrt{2}}$. Subsequently, we compute $\epsilon(\rho_2)$ and $\epsilon(\rho_3)$ using the following equations.

$$\epsilon(\rho_2) = \epsilon(|p\rangle\langle p|) + i\epsilon(|m\rangle\langle m|) - (1+i)\frac{(\epsilon(\rho_1) + \epsilon(\rho_4))}{2}, \quad (8)$$

$$\epsilon(\rho_3) = \epsilon(|p\rangle\langle p|) - i\epsilon(|m\rangle\langle m|) - (1-i)\frac{(\epsilon(\rho_1) + \epsilon(\rho_4))}{2}. \quad (9)$$

We have used the above scheme to perform QPT of all the single-qubit gates on IBM's quantum processors IBM QX4 (for all the possible positions of the gates) and IBM QX2 (while the gate to be tomographed is placed in the third qubit line only). Results of QPT has been reported in Sec. 4 and summarized in Table 3 for IBM QX4 processor and in Table 4 for IBM QX2 processor.

3.2. QPT of C-NOT

In the following, we discuss QPT of C-NOT gates used in the IBM QX4 processor. The only two-qubit gate that can be imple-
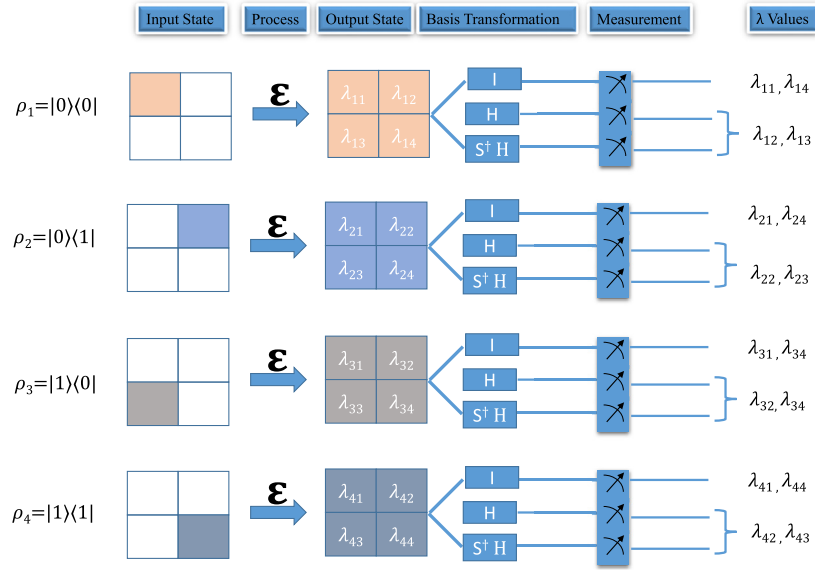
Fig. 1. Scheme for performing single-qubit QPT on IBM's quantum processors. The first column shows input state initialized to basis ρ_j followed by application of the quantum operation $\epsilon(\rho)$ as mentioned in the second column. The Third column contains output states ρ_k as a result of application of quantum operation. The fourth and fifth columns are steps of standard procedure for quantum state tomography [3,41,42]. The fourth column contains gates/combination of gates used to transfer unobservable non-diagonal elements $\langle X \rangle$ and $\langle Y \rangle$ into observable diagonal elements while the fifth column shows measurement in Z basis. Measurement outcomes obtained from three experiments are shown in the last column.

Table 3
Fidelities of experimental χ matrices with theoretical χ matrices for all the single-qubit gates that can be implemented in IBM QX4 quantum processor. The first row is qubit index q[i] as mentioned in IBM quantum computer. Corresponding gates for rows numbers (2-9) are: $\mathbb{I}$, X, Y, Z, H, T, T†, S, and S†.

Qubit number q[i]	q[0]	q[1]	q[2]	q[3]	q[4]
$\mathbb{I}$	0.9260	0.9073	0.9540	0.9090	0.8872
X	0.9093	0.8850	0.9535	0.8958	0.8855
Y	0.9145	0.8890	0.9515	0.8930	0.8845
Z	0.8222	0.8925	0.9573	0.9042	0.8920
H	0.9120	0.8750	0.9650	0.8990	0.9045
T	0.9111	0.9150	0.9611	0.8846	0.8975
T†	0.9049	0.9391	0.9604	0.8688	0.7841
S	0.8978	0.9147	0.9560	0.8958	0.8978
S†	0.9045	0.9445	0.9603	0.8885	0.7948

mented directly in IBM QX2 and IBM QX4 was CNOT. For our experiments, we have used IBM QX4 version of the processor (now it has been changed to IBM Q5 tenerife). This 5-qubit quantum processor used to allow direct implementation of C-NOT gates in six configurations out of total 20 possible configurations. We have performed QPT of C-NOT gates only for three such positions as that would be enough to establish our point. These configurations are

1. Qubit q[1] as control and q[0] as target i.e., $C_1 N_0$.
2. Qubit q[2] as control and q[0] as target i.e., $C_2 N_0$.
3. Qubit q[3] as control and q[2] as target i.e., $C_3 N_2$.

Following the theory of QPT as explained in Sec. 2 we have computed the relevant χ matrices. For the purpose of computing χ matrices, we choose input basis as $\rho_i = \{|00\rangle\langle 00|, |00\rangle\langle 01|, |00\rangle\langle 10|, |00\rangle\langle 11|, |01\rangle\langle 00|, |01\rangle\langle 01|, |01\rangle\langle 10|, |01\rangle\langle 11|, |10\rangle\langle 00|, |10\rangle\langle 01|, |10\rangle\langle 10|, |10\rangle\langle 11|, |11\rangle\langle 00|, |11\rangle\langle 01|, |11\rangle\langle 10|, |11\rangle\langle 11|\}$, for $i = 1 : 16$ and fixed set of operators $\tilde{E} = \{II, IX, -iIY, IZ, XI, XX, -iXY, XZ, -iYI, -iYX, -iYY, -iYZ, ZI, ZX, -iZY, ZZ\}$.

Further, we followed the steps demonstrated in Sec. 2 (i.e., to initialize a two-qubit system under consideration into input basis ρ_i followed by application of process ϵ and ultimately performing QST of two-qubit output states ρ_j) to get all the λ_{ij} values. Further,

we compute β matrix using ρ_i, ρ_j, $\tilde{E_m}$, and $\tilde{E_n}$ and ultimately χ matrix. QST of output matrix for C-NOT gate.

Similar to single-qubit QPT case, also in case of C-NOT gate initialization of non-Hermitian input states i.e., $\rho_i - \{|00\rangle\langle 00|, |01\rangle\langle 01|, |10\rangle\langle 10|, |11\rangle\langle 11|\}$ are not allowed which restricts further application of QPT, instead we use appropriate linear combination of elements from the following set of physical states (i.e., $|0\rangle\langle 0| \otimes |p\rangle\langle p|, |0\rangle\langle 0| \otimes |m\rangle\langle m|, |1\rangle\langle 1| \otimes |p\rangle\langle p|, |1\rangle\langle 1| \otimes |m\rangle\langle m|, |p\rangle\langle p| \otimes |0\rangle\langle 0|, |m\rangle\langle m| \otimes |0\rangle\langle 0|, |p\rangle\langle p| \otimes |1\rangle\langle 1|, |m\rangle\langle m| \otimes |1\rangle\langle 1|, |p\rangle\langle p| \otimes |m\rangle\langle m|, |m\rangle\langle m| \otimes |p\rangle\langle p|, |p\rangle\langle p| \otimes |p\rangle\langle p|, |m\rangle\langle m| \otimes |m\rangle\langle m|)$ in order to realize input states with the help of formula used in Eq. (9).

4. Results and discussions

Following the procedure described in the previous section, QPT for various single-qubit gates and C-NOT gates in three configurations that can be realized on IBM's quantum computing architectures have been performed. Representative results for IBM QX4 are illustrated in Fig. 2, Fig. 3, Fig. 4, and Fig. 5. These results can be used to compute fidelity. In fact, fidelity [18] of experimentally obtained χ matrices with the theoretical ones may be viewed as the gate fidelity and it has been computed by using the following formula

$$F(\chi_{th}, \chi_{exp}) = \frac{\text{Tr}(\chi_{exp}\chi_{th}^\dagger)}{\sqrt{\text{Tr}\chi_{th}^\dagger\chi_{th}}\sqrt{\text{Tr}\chi_{exp}^\dagger\chi_{exp}}}. \quad (10)$$

Here, χ_{th} and χ_{exp} are theoretical and experimental χ matrices, respectively. For single-qubit case, we perform QPT of all the gates namely, (a) $\mathbb{I}$, (b) X, (c) Y, (d) Z, (e) T, (f) T†, (g) S, (f) S† for all qubit lines for IBM QX4 architecture and for the third qubit line (i.e., q[2]) for IBM QX2. Fidelities for all the single-qubit gates and for all the possible qubit lines for IBM QX4 are given in Table 3. Similarly, in Table 4, we provide the results for IBM QX2. In Fig. 2, we show real and imaginary part of χ matrix for H gate on third-qubit for both processors. χ matrices for IBM QX2 with fidelity $F_H = 0.9650$ are shown in middle trace and for IBM QX4 with fidelity $F_H = 0.6060$ are shown in lower trace. Furthermore, in Fig. 3

Table 4

Fidelities of experimental χ matrices with theoretical χ matrices for all the single-qubit gates are obtained by placing the on the third-qubit line in IBM QX2 processor. Corresponding gates for columns (2-9) are: $\mathbb{I}$, X, Y, Z, H, T, $T^\dagger$, S, and $S^\dagger$.

Gates	$\mathbb{I}$	X	Y	Z	H	T	$T^\dagger$	S	$S^\dagger$
Fidelities	0.4855	0.4792	0.9487	0.7190	0.6060	0.9453	0.4746	0.9317	0.9419
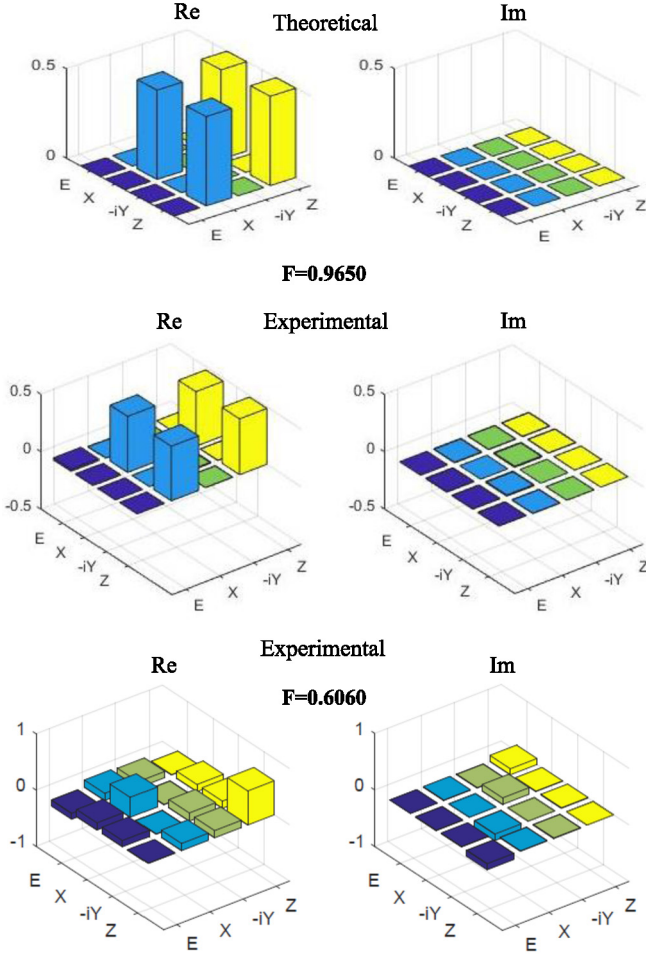
Fig. 2. χ matrices for Hadamard gate obtained from standard quantum process tomography procedure. For the purpose of comparison theoretical χ matrices (top trace) and experimental matrices for both IBM QX4 (middle trace) and IBM QX2 (bottom trace) respectively. Left and right columns contain real and imaginary parts of χ matrix. Fidelity of the Hadamard gates in the two architectures are 0.9650 and 0.6060.
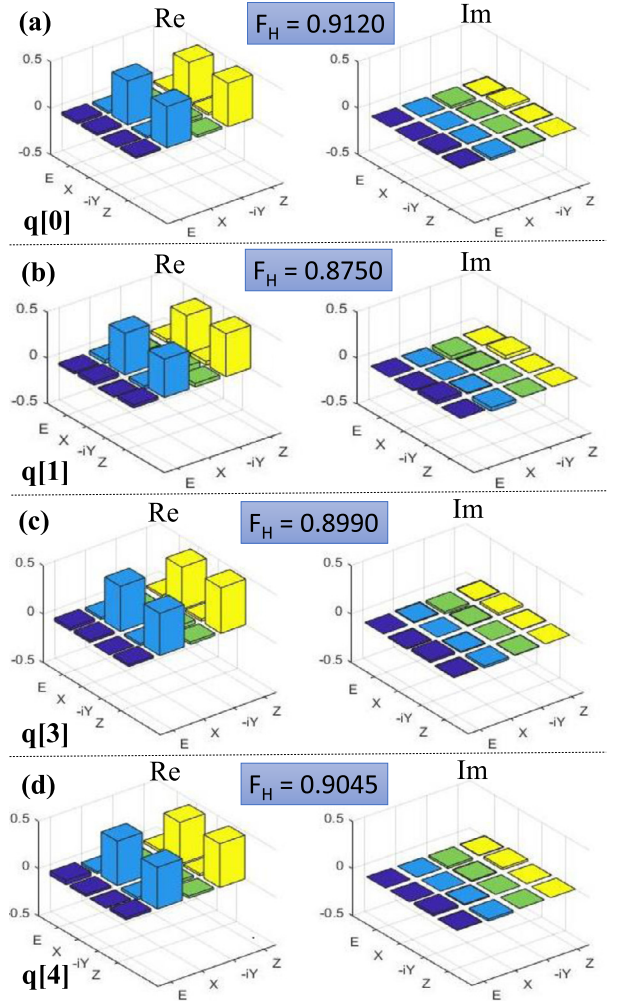

Fig. 3. χ matrices for Hadamard gate applied on different qubits. (a) q[0], (b) q[1], (c) q[3], (d) q[4]. Real and imaginary parts of χ matrix are arranged as in Fig. 2.

we report real and imaginary part of χ matrices for H applied on all qubits along with their fidelities. Real and imaginary part of χ matrices for all the gates applied on third-qubit, for IBM QX2 architecture are shown in Fig. 4. Results of QPT have been summarized in Table 4 for IBM QX2 processor and in Table 3 for IBM QX4 processor. Comparing the values of fidelity mentioned in these two tables, one can easily conclude that the IBM QX2 would usually perform better than IBM QX4, as IBM QX4's gate fidelity is always higher than that of IBM QX2 (except for the case of Y gate. Similarly, in case of two-qubit gates we have performed QPT of C-NOT gates C_1N_0, C_2N_0, and C_3N_2. The χ matrices obtained for these C-NOT gates are shown in Fig. 5. Top trace contains theoretical χ matrices, upper middle trace contains experimental χ matrix of C_1N_0, lower middle trace contains experimental χ matrix of C_2N_0, and bottom trace contains experimental χ matrix of C_3N_2. Left column in Fig. 5 corresponds to the real part of χ matrix and right column corresponds to imaginary part of χ matrix. Fidelity of C-NOT gates are obtained as $f_{C_3N_2} = 0.8266$,

$f_{C_1N_0} = 0.7092$, and $f_{C_2N_0} = 0.6973$, which does not appear to be high. However, to have a feeling of the quality of the gates realized in IBM quantum processors, the comparison should actually be made with the other technologies. In what follows, we have tried to do so.

We may compare our results with other reported QPT results to develop a feeling about the quality (goodness) of single-qubit gates that can be implemented in IBM's quantum computing architecture. For example, single-qubit gate fidelity, in superconducting qubit based architecture has been reported as 0.98 [43], in nitrogen vacancy center based architecture has been reported as 0.99 [44], and average fidelity of single-qubit gates in nuclear magnetic resonance architecture has been reported as 0.98 [20]. A glance on our results reveals H gate on third-qubit line has the best gate fidelity with maximum fidelity of 0.97 (cf. Fig. 2). A comparison of IBM's best gate fidelity with gate fidelities achieved in other architectures reveal that the quality of the gates implemented in IBM quantum processors are lower in comparison to other architectures. Similarly, fidelity of C-NOT gate in NMR architecture is '0.99 while in
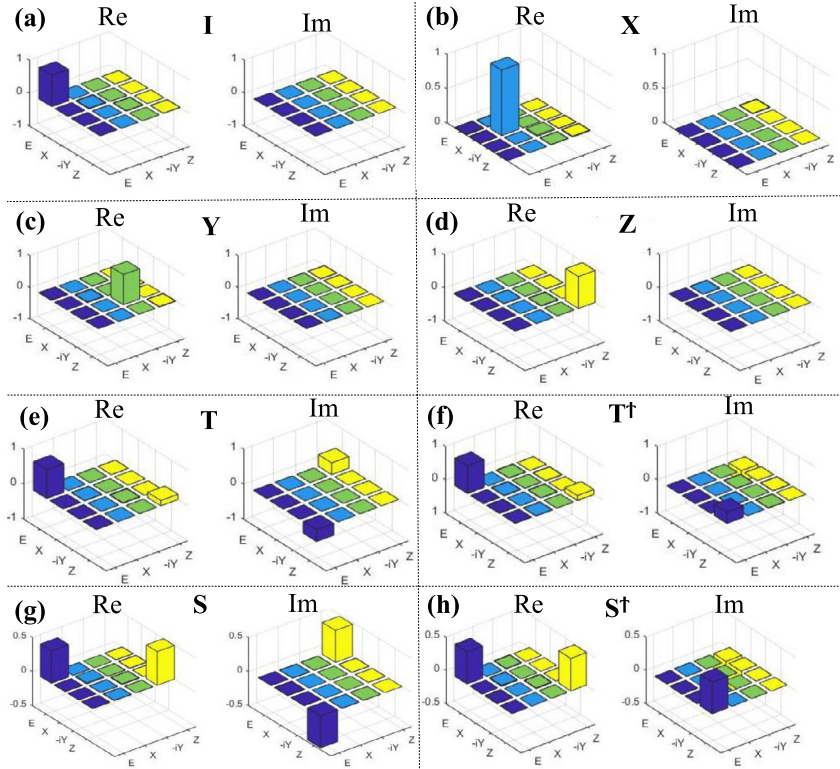
Fig. 4. χ matrices for various single-qubit gates in IBM's gate library i.e., Clifford+T library applied on qubit q[2] of IBM QX4 processor. (a) $\mathbb{I}$, (b) X, (c) Y, (d) Z, (e) T, (f) T†, (g) S, (f) S†. Again real and imaginary parts of χ matrix are arranged as in Fig. 2.

NV center architecture it is 0.98. Although there are several process tomography techniques and which one to use is subject of their best applicability, unfortunately measures for the goodness of gates used in these techniques are not monotone of each other, so a direct comparison of gate fidelities from two techniques (for example as in present case Randomized Bench Marking [13] and standard QPT [1]) is neither feasible [45] nor is the aim of the present study, instead we just wish to report bad quality of single-qubit gates as revealed by standard quantum process tomography. Just to get a glimpse of the merit of the output quantum states in our QPT experiments, we have calculated their fidelities which range from 0.9120 to 0.9741 and is consistent with the fidelities measured in some other works (see ref., [34] and [40]), demonstrated using IBM quantum processor. To estimate the goodness of the linear process map we also calculate the variance of input vector (v_1) and output vectors (v_2) of the map (maps output QST data to χ matrix representation). As an example, the two variance (v_1) and v_2 for Hadamard gate on qubit $q[2]$ are = 0.2524 and (= 0.2524). Furthermore, to calculate fluctuations in the QST data and QPT data ascribed to gate error and measurement error we have 18 times repeated the QPT experiment with Hadamard gate applied on qubit $q[2]$. The QST data, for state $|0\rangle\langle0|$ has standard deviation of 4.6452×10^{-4} around mean fidelity of 0.9988, and for state $|1\rangle\langle1|$ has standard deviation of 3.3212×10^{-4} around mean fidelity of 0.9991.

5. Conclusions

IBM quantum computers allow a user to utilize gates from the Clifford+T gate library with some restrictions on the applicability of CNOT gates based on the selected architecture. In this work, we have performed QPT for all the quantum gates that can be directly implemented in IBM QX2 and IBM QX4 architectures. Specifically, QPT has been performed and thus gate fidelity is computed for

(i) all the single-qubit gates in all possible positions (i.e., gate fidelity is computed by placing each of the gates in all five qubit lines) in the IBM QX4 architecture, (ii) all the single qubit gates placed individually in the third qubit line in IBM QX2 architecture and (iii) CNOT gates in IBM QX4 architecture in three allowed configurations namely, C_1N_0, C_2N_0, C_3N_2. The obtained gate fidelities show that except for the Y gate, the fidelity of the quantum gates implemented in IBM QX4 is better than the same in IBM QX2. Further, it's observed that the obtained gate fidelity is often lower than the corresponding values obtained earlier using NMR and other technologies. Specially, fidelities of CNOT gates are found to be really low. Only C_3N_2 has a reasonably good fidelity. This is what has led to lower state fidelity in various cases reported earlier. Further this limitation of the gates has restricted the maximum number gates that can be applied in a particular architecture of IBM quantum computers. Although, considering the possibility of large contribution from measurement error in the overall low fidelity of various gates especially in case of the CNOTs it is hard to say that bad fidelity is because of error in control fields or due to measurement error but certainly the aggregate effect leads to a final low fidelity quantum state. Results of our study points out the need of further improvization of IBM gates which are robust against not only decoherence but also against many other experimental varaying parameters like microwave inhomogeinity. Which demands using numerically optimized gates and decoherence protected gates. This indicates a possibility of improvization in the superconductivity-based technology used in IBM quantum computers in their journey towards building a scalable quantum computer. Keeping these points in mind, we conclude this article with an optimistic view that the present work will not only provide physical insights into the earlier reported results, but by pointing out the possibility of improvization also contribute to the future development of the related technologies.
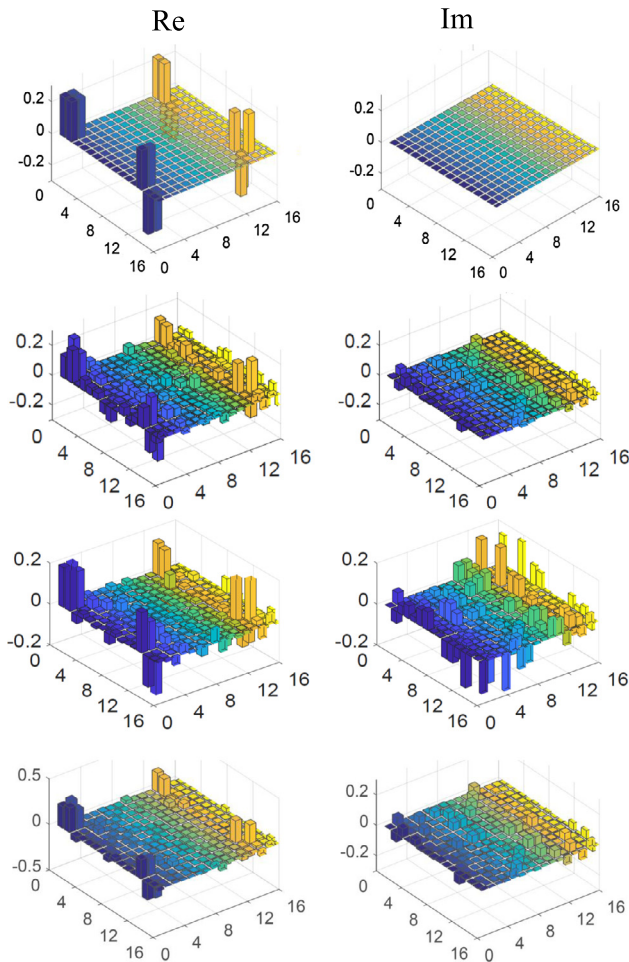
Fig. 5. χ matrices for various C-NOT gates in IBM's QX4 processor. Theoretical χ matrices in the top trace. χ matrices for C_1N_0 gate in the upper middle trace. χ matrices for C_2N_0 gate in the lower middle trace. χ matrices for C_3N_2 gate in the bottom trace.

Declaration of competing interest

This is to state that the authors of the present paper does not have any conflict of interest with any one.

Acknowledgements

References

[1] I.L. Chuang, M.A. Nielsen, Prescription for experimental determination of the dynamics of a quantum black box, J. Mod. Opt. 44 (1997) 2455–2467.

[2] J. Poyatos, J.I. Cirac, P. Zoller, Complete characterization of a quantum process: the two-bit quantum gate, Phys. Rev. Lett. 78 (1997) 390–393.

[3] I.L. Chuang, N. Gershenfeld, M.G. Kubinec, D.W. Leung, Bulk quantum computation with nuclear magnetic resonance: theory and experiment, Proc. R. Soc. Lond. Ser A 454 (1998) 447.

[4] A.M. Childs, I.L. Chuang, D.W. Leung, Realization of quantum process tomography in NMR, Phys. Rev. A 64 (2001) 012314.

[5] Y.S. Weinstein, T.F. Havel, J. Emerson, et al., Quantum process tomography of the quantum Fourier transform, J. Chem. Phys. 121 (2004) 6117–6133.

[6] F. De Martini, A. Mazzei, M. Ricci, G.M. D'Ariano, Exploiting quantum parallelism of entanglement for a complete experimental quantum characterization of a single-qubit device, Phys. Rev. A 67 (2003) 062307.

[7] J.B. Altepeter, D. Branning, E. Jeffrey, et al., Ancilla-assisted quantum process tomography, Phys. Rev. Lett. 90 (2003) 193601.

[8] J.L. O'Brien, G.J. Pryde, A. Gilchrist, et al., Quantum process tomography of a controlled-NOT gate, Phys. Rev. Lett. 93 (2004) 080502.

[9] M.W. Mitchell, C.W. Ellenor, S. Schneider, A.M. Steinberg, Diagnosis, prescription, and prognosis of a Bell-state filter by quantum process tomography, Phys. Rev. Lett. 91 (2003) 120402.

[10] M. Riebe, K. Kim, P. Schindler, et al., Process tomography of ion trap quantum gates, Phys. Rev. Lett. 97 (2006) 220407.

[11] D. Hanneke, J.P. Home, J.D. Jost, et al., Realization of a programmable two-qubit quantum processor, Nat. Phys. 6 (2010) 13.

[12] M. Neeley, M. Ansmann, R.C. Bialczak, et al., Process tomography of quantum memory in a Josephson-phase qubit coupled to a two-level state, Nat. Phys. 4 (2008) 523.

[13] J.M. Chow, J.M. Gambetta, L. Tornberg, et al., Randomized benchmarking and process tomography for gate errors in a solid-state qubit, Phys. Rev. Lett. 102 (2009) 090502.

[14] R.C. Bialczak, M. Ansmann, M. Hofheinz, et al., Quantum process tomography of a universal entangling gate implemented with Josephson phase qubits, Nat. Phys. 6 (2010) 409.

[15] T. Yamamoto, M. Neeley, E. Lucero, et al., Quantum process tomography of two-qubit controlled-Z and controlled-NOT gates using superconducting phase qubits, Phys. Rev. B 82 (2010) 184515.

[16] J.M. Chow, A.D. Córcoles, J.M. Gambetta, et al., Simple all-microwave entangling gate for fixed-frequency superconducting qubits, Phys. Rev. Lett. 107 (2011) 080502.

[17] A. Dewes, F.R. Ong, V. Schmitt, et al., Characterization of a two-transmon processor with individual single-shot qubit readout, Phys. Rev. Lett. 108 (2012) 057002.

[18] J. Zhang, A.M. Souza, F.D. Brandao, D. Suter, Protected quantum computing: interleaving gate operations with dynamical decoupling sequences, Phys. Rev. Lett. 112 (2014) 050502.

[19] M. Howard, J. Twamley, C. Wittmann, et al., Quantum process tomography and linblad estimation of a solid-state qubit, New J. Phys. 8 (2006) 33.

[20] A. Shukla, T. Mahesh, Single-scan quantum process tomography, Phys. Rev. A 90 (2014) 052301.

[21] I. Pogorelov, G. Struchalin, S. Straupe, et al., Experimental adaptive process tomography, Phys. Rev. A 95 (2017) 012302.

[22] M. Branderhorst, J. Nunn, I. Walmsley, R. Kosut, Simplified quantum process tomography, New J. Phys. 11 (2009) 115010.

[23] Z. Wu, S. Li, W. Zheng, X. Peng, M. Feng, Experimental demonstration of simplified quantum process tomography, J. Chem. Phys. 138 (2013) 024318.

[24] V. Dobrovitski, G. De Lange, D. Riste, R. Hanson, Bootstrap tomography of the pulses for quantum control, Phys. Rev. Lett. 105 (2010) 077601.

[25] A. Gaikwad, D. Rehal, A. Singh, K. Dorai, et al., Experimental demonstration of selective quantum process tomography on an NMR quantum information processor, Phys. Rev. A 97 (2018) 022311.

[26] M. Mohseni, D. Lidar, Direct characterization of quantum dynamics, Phys. Rev. Lett. 97 (2006) 170501.

[27] IBM Quantum Computing Platform, http://research.ibm.com/ibm-q/qx/, 2016. (Accessed 4 May 2016).

[28] Ibmqx2 quantum processor, https://quantumexperience.ng.bluemix.net/qx/editor, 2016.

[29] S.J. Devitt, Performing quantum computing experiments in the cloud, Phys. Rev. A 94 (2016) 032329.

[30] Y. Wang, Y. Li, Z.-q. Yin, B. Zeng, 16-qubit IBM universal quantum computer can be fully entangled, arXiv preprint arXiv:1801.03782, 2018.

[31] A. Kandala, A. Mezzacapo, K. Temme, et al., Hardware-efficient variational quantum eigensolver for small molecules and quantum magnets, Nature 549 (2017) 242.

[32] M. Dall'Arno, F. Buscemi, V. Vedral, Device-independent inference of physical devices: theory and implementation, arXiv preprint arXiv:1805.01159, 2018.

[33] M. Sisodia, A. Shukla, K. Thapliyal, A. Pathak, Design and experimental realization of an optimal scheme for teleportation of an n-qubit quantum state, Quantum Inf. Process. 16 (2017) 292.

[34] M. Sisodia, A. Shukla, A. Pathak, Experimental realization of nondestructive discrimination of Bell states using a five-qubit quantum computer, Phys. Lett. A 381 (2017) 3860–3874.

[35] S. Satyajit, K. Srinivasan, B.K. Behera, P.K. Panigrahi, Discrimination of highly entangled Z-states in IBM quantum computer, Quantum Inf. Process. 17 (2017) 212.

[36] IBMQX2 Architecture, https://github.com/IBM/qiskit-qx-info/blob/master/backends/IBMqx2/README.md, 2017.

[37] M.A. Nielsen, I.L. Chuang, Quantum Computation and Quantum Information, Cambridge University Press, 2010.

[38] IBMQX4 Architecture, https://github.com/IBM/qiskit-qx-info/blob/master/backends/IBMqx4/README.md, 2017.

[39] B.K. Behera, A. Banerjee, P.K. Panigrahi, Experimental realization of quantum cheque using a five-qubit quantum computer, Quantum Inf. Process. 16 (2017) 312.

[40] B.K. Behera, T. Reza, A. Gupta, P.K. Panigrahi, Designing quantum router in IBM quantum computer, arXiv preprint arXiv:1803.06530, 2018.

[41] D.G. Cory, R. Laflamme, E. Knill, et al., NMR based quantum information processing: achievements and prospects, Fortschr. Phys. 48 (2000) 875–907.

[42] D.G. Cory, A.F. Fahmy, T.F. Havel, Ensemble quantum computing by nmr spectroscopy, Proc. Natl. Acad. Sci. USA 94 (1997) 1634.

[43] E. Lucero, M. Hofheinz, M. Ansmann, et al., High-fidelity gates in a single Josephson qubit, Phys. Rev. Lett. 100 (2008) 247001.

[44] M.W. Doherty, N.B. Manson, P. Delaney, et al., The nitrogen-vacancy colour centre in diamond, Phys. Rep. 528 (2013) 1.

[45] M. Mohseni, A. Rezakhani, D. Lidar, Quantum-process tomography: resource analysis of different strategies, Phys. Rev. A 77 (2008) 032322.